Streamer tomography velocity models for the Gulf of Corinth and Gulf of Itea, Greece

Barry R Zelt, Brian R Taylor, Jonathan R Weiss, Andrew M Goodliffe, Maria M Sachpazi, Alfred Hirn

Geophys. J. Int. (2004) **159,** 333–346 doi: 10.1111/j.1365-246X.2004.02388.x

Streamer tomography velocity models for the Gulf of Corinth and Gulf of Itea, Greece

Barry C. Zelt,[1] Brian Taylor,[1] Jonathan R. Weiss,[1] Andrew M. Goodliffe,[1,*] Maria Sachpazi[2] and Alfred Hirn[3]

[1] *School of Ocean and Earth Science and Technology, University of Hawaii,* 1680 *East-West Road, Honolulu, HI* 96822, *Hawaii, USA. E-mail: bzelt@soest.hawaii.edu*

[2] *Geodynamic Institute, National Observatory of Athens, Athens, Greece*

[3] *Laboratoire de Sismologie Expérimentale, Département de Sismologie, Institut de Physique du Globe de Paris, Paris, France*

Accepted 2004 June 18. Received 2004 June 16; in original form 2004 February 25

SUMMARY

The Gulf of Corinth (GOC), Greece is a rapidly extending, active continental rift with a record of large, damaging earthquakes. An extensive multichannel seismic (MCS) survey of the GOC conducted in 2001 provided, in addition to the processed MCS images, the opportunity to constrain velocity structure using refracted arrivals recorded along a 6-km-long streamer. We use first-arrival traveltimes to derive tomographic *P*-wave velocity models for several profiles collected in the central portion of the GOC. Eight of the profiles are closely spaced, north–south lines crossing the GOC and extending into the Gulf of Itea (GOI); a ninth profile is an east–west-oriented tie line. The N–S profiles image the relatively simple velocity structure of the deep Corinth rift basin and more complicated structure of the northern margin of the currently active rift. Integration of the velocity models with migrated MCS sections shows that south of the GOI the basement, which comprises Mesozoic nappes, occurs at a velocity of 4.5 km s^{-1} in the velocity models, although the actual velocity at, or just below, the top of basement is probably closer to 5–5.5 km s^{-1}. The maximum sediment thickness in the Corinth basin is 2.2 km. The basement shallows to the north into a fault-bounded terrace in the central region between the two gulfs. Sediment cover in this central region decreases in thickness from west to east. Beneath the GOI, low average velocities beneath the rift-onset reflector indicate the presence of pre-rift sediments. The pre-rift velocity structure in the GOI is complex, with significant lateral variation from west to east. The E–W line shows that high-velocity basement is shallow ($\leq$1 km depth) and flat to the west of the GOI but dips $\sim$20° east down to $\sim$1.5 km beneath the pre-rift sediments of the GOI.

Key words: basement, Greece, Gulf of Corinth, streamer, tomography, velocity.

1 INTRODUCTION

The Gulf of Corinth (GOC), which separates the Peloponnisos from central Greece, is an active continental rift within the Aegean, which itself is one of the most active extensional continental regions in the world (Armijo *et al.* 1996). The GOC has a well-documented history of large earthquakes, including an $Ms = 6.2$ event in 1995 that severely damaged the city of Aigion. Focal mechanisms from 10 large earthquakes in the last 35 yr show a pattern of E–W-trending normal faulting, consistent with geodetic measurements that show extension is directed north–south across the gulf, and that deformation is mainly localized beneath the gulf (Clarke *et al.* 1997; Davies *et al.* 1997; Clarke *et al.* 1998; Billiris *et al.* 1991; Briole *et al.* 2000; Avallone *et al.* 2004). There is, however, considerable debate concerning the geometry of crustal faulting that is accommodating the deformation, especially in light of focal mechanisms (Hatzfeld *et al.* 1996) and microseismicity studies (Rietbrock *et al.* 1996; Rigo *et al.* 1996), which suggest that, in the western and central parts of the gulf, slip may be occurring on low-angle (15–35°) normal faults.

A recent study of the rift structure using multichannel seismic (MCS) data (Sachpazi *et al.* 2003) sheds light on the basement topography, basin infill and active faulting, but only along three profiles. To provide a more complete picture that can be used to establish the mechanics of active continental extension requires a far greater spatial coverage in this highly complex region. To this end, in 2001 July the University of Hawaii, National Observatory of Athens and Institut de Physique du Globe de Paris conducted an extensive MCS survey of the GOC, collecting a dense grid of

*Now at: Department of Geological Sciences, University of Alabama, Tuscaloosa, Alabama, USA.

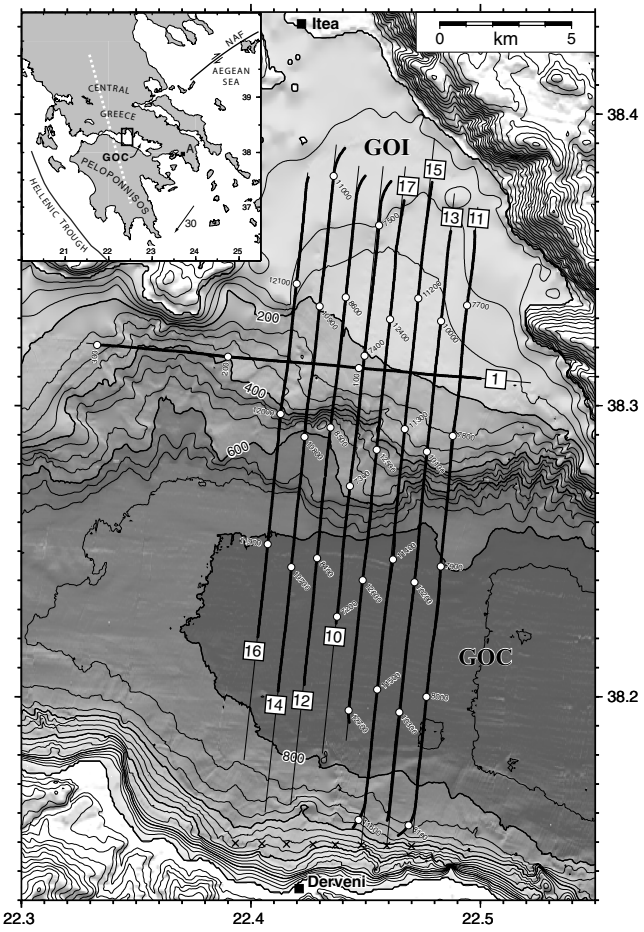

Figure 1. Bathymetry map and shot lines. Bathymetry data were collected during the cruise using the Hydrosweep DS2 multibeam sonar of the R/V Ewing. Contour interval for bathymetry is 50 m. Heavy black lines, which are actually closely spaced dots, show shot points used in this study. Every 100th shot point is identified (numbers next to white circles). Numbers within squares identify the lines. Thin black lines beneath, and extending beyond, the shot points show the extent of each 2-D model. X symbols near the bottom of the plot represent the model origins for the north–south lines; the origin for line 1 is off this map (at 22.20292°E, 38.33004°N). GOC, Gulf of Corinth; GOI, Gulf of Itea. Inset map shows the regional setting for this study. Rectangle marks region of main map. Broken white line shows trend of the Hellenic mountain belt. Numbered arrow indicates direction and rate (mm yr^{-1}) of extension in the Aegean region relative to Eurasia. The African Plate, not shown on this map, is moving north at approximately 6 mm yr^{-1} relative to Eurasia (McClusky *et al.* 2000). A, Athens; NAF, North Anatolian fault.

∼50 seismic lines using the R/V Maurice Ewing (Goodliffe *et al.* 2003; Taylor *et al.* 2003; Weiss *et al.* 2003). Eight of these lines (Fig. 1) are north–south-oriented dip lines extending across the central GOC into the Gulf of Itea (GOI). The close spacing of these lines (∼1 km) and the fact that they extend across the northern border of the main rift basin provide an opportunity for revealing, in an almost 3-D sense, the structures accommodating deformation. Ideally, in addition to the MCS images, one would like to have accurate velocity models, which are essential for pre-stack depth migration and time-to-depth conversions. Also, because persistent water-column-generated multiples, of both the primary and peg-leg variety, obfuscate some of the primary reflections, particularly in shallow-water regions such as the GOI, velocity models can be used to discriminate between low-velocity sediments and high-velocity basement rocks.

In this paper, we derive 2-D models for the shallow *P*-wave velocity structure beneath nine MCS lines: eight north–south lines previously mentioned and an east–west tie line along the northern margin of the GOC, extending into the GOI. We refer to the method used as streamer tomography, by which we mean that, for each line, we perform a standard 2-D tomographic inversion using first-arrival traveltimes recorded along the seismic streamer. In many respects, our approach is similar to that of Calvert *et al.* (2003) who applied tomographic inversion to streamer data from Puget Sound, Washington. In comparison, our study region is structurally more complicated: the range of water depths is greater, maximum water depth is deeper and the range of velocities encountered is much greater as a result of a shallow high-velocity basement.

2 GEOLOGICAL AND TECTONIC SETTING

The Corinth rift is the southernmost of a series of NW–SE to E–W-oriented active graben that discontinuously link the western part of the North Anatolian fault to the Hellenic subduction zone (Briole *et al.* 2000; Fig. 1 inset). Extension throughout the Aegean started in the late Oligocene (Jolivet 2001). There are multiple likely causes of present-day extension, including gravitational instability of the Neogene Hellenic mountains, roll-back of the African Plate that is subducting beneath the European Plate at approximately 6 mm yr^{-1} (McClusky *et al.* 2000) and a response to accommodation of the western-propagating tip of the North Anatolian fault (Fig. 1 inset; Armijo *et al.* 1996; Moretti *et al.* 2003).

The Corinth rift formed mainly during the Quaternary as suggested by E–W normal faults that cut sediments of Pliocene–Pleistocene age (Armijo *et al.* 1996). The current extension rate varies, decreasing from 16 mm yr^{-1} in the west to 11 mm yr^{-1} in the east (Avallone *et al.* 2004). The width of the gulf decreases from east to west suggesting there has been greater extension in the east despite the present lower extension rate. The direction of extension also varies, but is, on average, approximately N–S. In addition to extension, the south coast is uplifting whereas the north coast is subsiding. The Corinth rift cuts obliquely across the NNW–SSE-trending fabric of the Hellenic mountain belt (Fig. 1 inset). The Mesozoic nappes of this belt form the basement of the gulf (Le Pourhiet *et al.* 2003). *P*-wave velocity at the top of basement beneath both the western and eastern GOC is 5.1–5.4 km s^{-1} (Zelt *et al.* 2003).

The GOC is oriented WNW–ESE and is 120 km long and ∼20 km wide, with a maximum depth of 880 m. To first order, the rift appears to be an asymmetric half-graben with an uplifted southern footwall and a down-flexed northern hangingwall (Armijo *et al.* 1996). Both the north and south sides of the rift are characterized by normal faults. N-dipping faults along the southern coast tend to dip steeply (40–60°) where they outcrop on land. Minor, antithetic S-dipping faults occur along the northern coast (Goldsworthy *et al.* 2002). Synrift sediments are exposed on the southern shore; most of the northern side of the GOC is devoid of recent sediments (Le Pourhiet *et al.* 2003).

The GOC is very active seismically with both a history of repeated large earthquakes and a high level of background seismicity (Ambraseys & Jackson 1990). Focal depths of large earthquakes occur near the base of the seismogenic layer at 10–15 km depth (Rigo *et al.* 1996). Beneath the gulf, however, a microseismicity study

(Rigo *et al.* 1996) shows a clustering of microearthquakes, which soles out at approximately 10 km depth along a boundary dipping ∼15° northwards. This has been interpreted as a detachment zone across which stress is transferred from a lower semi-brittle zone to an upper brittle zone and into which root the steep (40–60°) N-dipping normal faults on the south side of the gulf. Alternatively, Hatzfeld *et al.* (2000) suggest that the cut-off in seismicity represents the seismic–aseismic transition.

3 SEISMIC DATA

Eight of the nine MCS lines (10–17) used in this study are dip lines that strike approximately 5° east of north (Fig. 1) and extend northwards into the GOI, which is one of a number of smaller, shallow (<200 m) gulfs adjoining the main GOC. The southern half of these lines straddle the western end of the Corinth deep, where water depths are greater than 800 m. The straight sections of these lines are 21–26 km long. Even number lines were shot from south to north; odd number lines were shot in the reverse direction. The ninth line, line 1, is an orthogonal tie line on the boundary between the two gulfs.

The data were acquired using the 6-km-long, 240-channel streamer of the R/V Maurice Ewing; the seismic source was a 20-gun tuned air gun array with a total volume of 138 L (8445 in^3). The data were acquired at a sample rate of 4 ms. Shot spacing was 50 m with an average time between shots of 21 s; receiver spacing along the streamer was 25 m. Except when the streamer was under the influence of a turn, the minimum and maximum shot–receiver offsets are typically 0.18 and 6.13 km, respectively. The spacing between north–south shot lines is approximately 950 m.

Because we employ a 2-D analysis procedure, we use only shots and receivers along the approximately linear parts of the shot lines, rejecting shot–receiver pairs collected when the ship was entering or exiting a turn. Even along the linear part of a shot line, the receiver feathering resulting from currents in the gulf can be quite large (Fig. 2). In some cases the deviation of the receivers from the shot line can be a large fraction of the line spacing; however, we did not eliminate any data resulting from feathering. The feathering will cause a small amount of blurring of the final 2-D tomographic images relative to an ideal 2-D acquisition geometry. True shot–receiver offsets were maintained in the 2-D analysis.

The quality of the seismic data seen on the shot gathers is generally very good but, not surprisingly, somewhat variable. In particular, data recorded near the center of the N–S lines, where the shot and receivers straddle the region between the GOI and GOC, are typically much noisier than along other parts of the line. This may, in part, be caused by the seafloor topography, which shoals rapidly from 800 to 200 m in this transition region, and/or it may signal that subsurface structural complexity is adversely affecting the propagation of seismic energy throughout this same region. Shot gathers recorded within the GOI also tend to be relatively complicated, making the correlation of the first-arrival phase more difficult compared with data recorded within the GOC.

An indication of lateral heterogeneity in the sedimentary and basement structure is exemplified by comparing record sections for shot gathers of adjacent lines. Within the GOC, record sections for lines 11, 13, 15 and 17 (Fig. 3) show a relatively strong phase with apparent velocity of approximately 3 km s^{-1} and, at offsets greater than ∼5.2 km, a very weak phase with an extremely high apparent velocity (>10 km s^{-1}) presumably associated with a south-dipping basement interface. For line 11, there is also a moderately strong

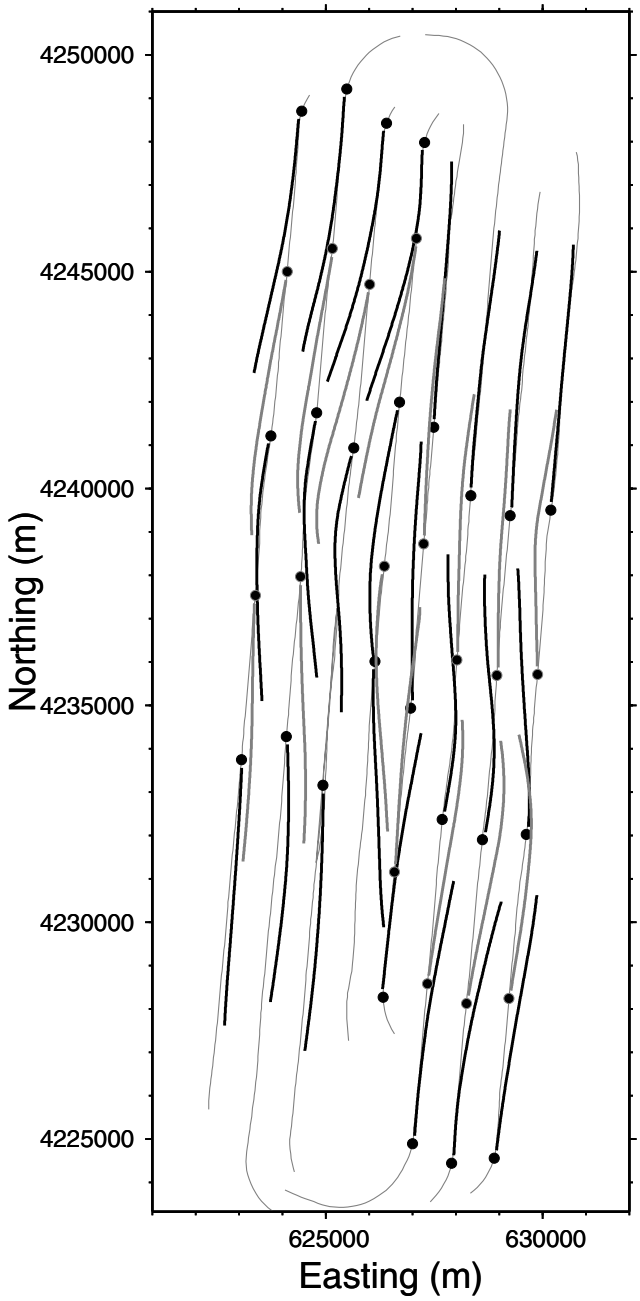

Figure 2. Streamer feathering during the experiment. The streamer (thick black and grey lines) and shot (black dots) locations for approximately every 50th shot are plotted on top of the shot tracks (thin grey lines). The maximum deviation of a receiver from its shot line is approximately 1 km, but typically the feathering is no more than a few hundred metres. *X* and *Y* axes are UTM (grid zone 34) easting and northing.

and coherent phase with an apparent velocity of ∼4.7 km s^{-1}, which appears as a first arrival between offsets of 4.9–5.6 km. This phase is not present, at least as a first arrival, on the other lines, including line 13, which is only 1 km further west. Within the GOI, the lateral heterogeneity is even more pronounced; adjacent record sections for lines 11, 13, 15 and 17 are markedly different (Fig. 4). Some of the first-arrival phases are very weak (e.g. the high apparent velocity phase at far offsets on lines 11 and 13) and there are delays between different branches of the first arrivals, suggestive of low-velocity zones (e.g. on line 17).

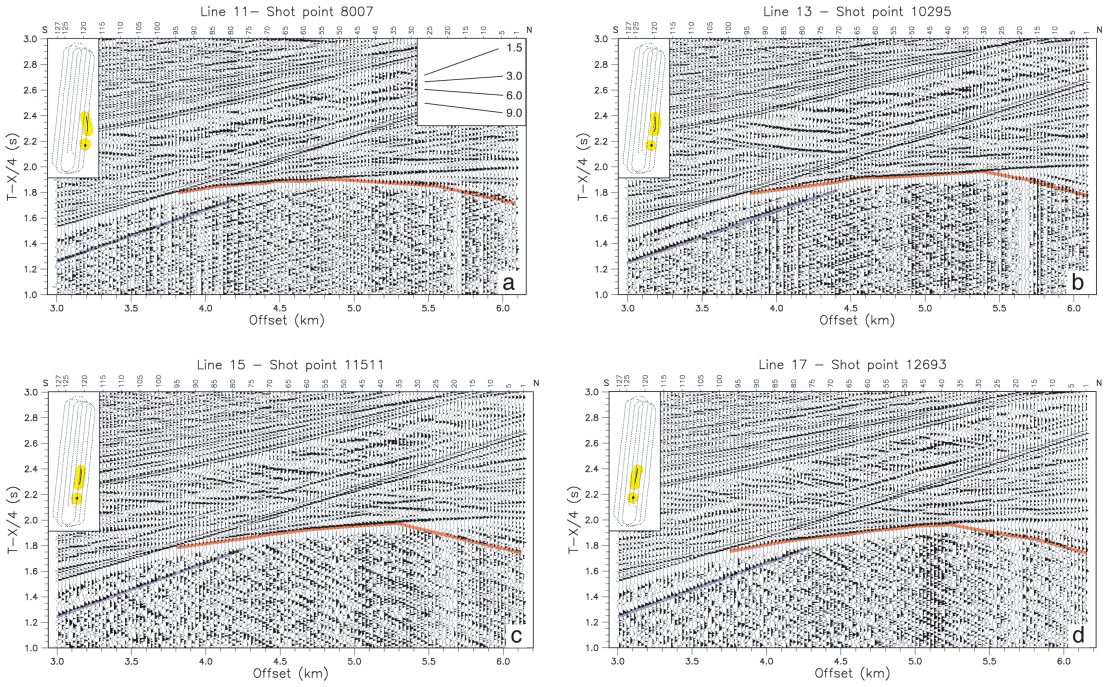

Figure 3. Shot gathers for four adjacent shots on (a) line 11, (b) line 13, (c) line 15 and (d) line 17. The shot and entire streamer lie within the Corinth deep. Red line indicates refracted first-arrival phase; blue line is the direct water wave. Only refractions that arrive ahead of the water wave (in time) are used in the modelling. Horizontal axis is shot–receiver offset; vertical axis is traveltime reduced at 4 km s^{-1}. Only offsets greater than 3 km are plotted. An automatic gain control (AGC) filter with a 100-ms window has been applied to boost up the first-arrival amplitudes, which are very weak in comparison with later phases. For comparison purposes the data are unfiltered; however, various bandpass filters were used to pick the data. Nomogram at top right in (a) illustrates moveout for phases of velocities between 1.5–9 km s^{-1}. Other nomograms show location of shot (dot) and receivers plotted (heavy line), both highlighted in yellow, in relation to the other north–south shot lines used in this study (dotted lines). Trace annotation at top is receiver channel number.

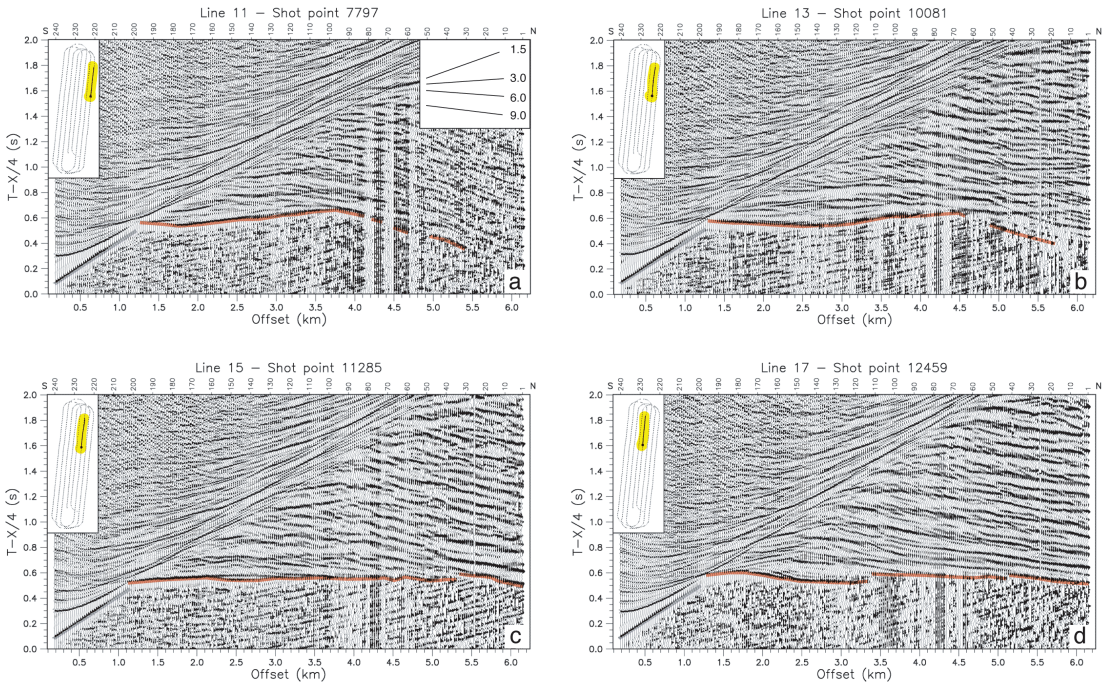

Figure 4. Shot gathers for four adjacent shots on (a) line 11, (b) line 13, (c) line 15 and (d) line 17. The shot and entire streamer lie within the Gulf of Itea. For all four gathers, the shot point was in 250-m-deep water. All 240 channels of the 6-km-long streamer are plotted. Red line indicates refracted first-arrival phase; blue line is the direct water wave. Only refractions that arrive ahead of the water wave (in time) are used in the modelling. Horizontal axis is shot–receiver offset; vertical axis is traveltime reduced at 4 km s^{-1}. An AGC filter with a 100-ms window has been applied to boost up the first-arrival amplitudes, which are very weak in comparison with later phases. For comparison purposes the data are unfiltered; however, various bandpass filters were used to pick the data. Nomogram at top right in (a) illustrates moveout for phases of velocities between 1.5–9 km s^{-1}. Other nomograms show location of shot (dot) and receivers plotted (heavy line), both highlighted in yellow, in relation to the other north–south shot lines used in this study (dotted lines). Trace annotation at top is receiver channel number.

The data used in the tomographic procedure are *P*-wave first-arrival traveltime picks. Only the first-arrival traveltimes of phases that arrive earlier than the direct water wave are used. Note that as the water depth beneath the shot and streamer increases, the crossover distance between the direct water wave and subseafloor refracted first arrivals increases as a result of the delay caused by the water. Thus with increasing water depth the number of useable data for tomography decreases and the depth range through which the refracted first arrivals turn is narrowed so that only the deepest refractions are available for imaging. For example, when both the shot and streamer are in the deepest water, the crossover point is at an offset of approximately 4.6 km, so that only the farthest 60 channels of the 240-channel streamer contain useful data (Fig. 3). In comparison, in relatively shallow water (150 m), the crossover point is at approximately 1.3 km (Fig. 4), so that the farthest 190 channels contain useful data. In shallow-water data it is possible to discern a number of refracted branches from sedimentary layers as well as basement; in deep water the shallow refracted phases are not first arrivals.

We picked first arrivals for every second shot, giving a shot spacing of 100 m for the tomographic inversions. Earlier work on an east–west-oriented line at the eastern end of the GOC (Zelt *et al.* 2003) showed us that the difference between final models derived using all shots versus every second shot was negligible. Picks of peak onsets were made the old fashioned way: by hand. On average, approximately 23 600 picks were obtained for each line. Pick uncertainties between 4–25 ms were calculated using an automated scheme based on the signal-to-noise ratio in a short (100 ms) time window around the pick (Zelt & Forsyth 1994). The overall average pick uncertainty is 9.6 ms (Table 1). Exemplary plots of all traveltime picks and uncertainties for line 15 are shown in Fig. 5. In Fig. 5(a), the picked times are presented as a traveltime field in which time along the streamer is plotted for each shot point. In this display, one can compare the variations in traveltime moveout from shot to shot and unpicked traces are easy to recognize. Gaps within the traveltime field represent noisy sections of the data that were not picked, or simply missed picks. The gap at the top of the plots represent the region where the direct water wave arrives ahead of the subseafloor refractions. The gap at the right arises because the streamer is involved in a turn and thus only times along the straight, near-offset part of the streamer are picked. The complexity of the traveltime field points to complexities in the underlying earth structure. The plot of pick uncertainties (Fig. 5b) reveals regions of relatively low uncertainty (e.g. between shots points 11 500–11 600) as well as more diffuse regions of high uncertainty.

Table 1. Data used to model each line and the goodness-of-fit statistics for the final models. Line, line number (the first eight lines are N–S lines listed west to east); No. shots, number of shot gathers from which data were obtained; No. picks, total number of data used in modelling; unc (ms), average uncertainty of picks; χ^2, normalized χ^2 misfit; dt_{rms} (ms), rms traveltime misfit.

Line	No. shots	No. picks	unc (ms)	χ^2	dt_{rms} (ms)
16	177	23932	8.9	1.11	7.8
14	210	25864	9.2	1.02	6.3
12	196	23906	9.4	1.80	9.4
10	170	22552	10.3	1.91	14.1
17	201	18800	9.4	1.86	14.6
15	249	26438	8.9	2.10	12.2
13	227	24905	8.3	1.00	7.5
11	234	23106	10.0	1.18	8.4
1	148	22631	8.1	1.00	6.4

4 METHOD

Our objective is to derive the smoothest 2-D velocity model for each line, i.e. with the least amount of required structure and with the best overall traveltime misfit; ideally with a normalized $\chi^2 = 1$. To do this, we use the first-arrival traveltime tomography method of Zelt & Barton (1998), with modifications to minimize the size and roughness of the perturbation from a background model. This method is iterative and requires a starting model; new ray paths are calculated for each iteration. For the forward step, traveltimes are calculated on a uniform 2-D velocity grid using a finite-difference solution to the eikonal equation (Vidale 1990), with modifications to handle large velocity gradients and contrasts (Hole & Zelt 1995). We use a 25-m grid for calculating traveltimes; all inversions are performed on a uniform 50-m grid. Grids extend from 0 (sea level) to 4 km depth; all depths mentioned in this paper are relative to sea level.

Bathymetry along each line was measured using Hydrosweep DS2 multibeam sonar. Average water velocity, based on temperature data from an expendable bathythermograph (XBT) probe launched near the mouth of the GOI, is 1.508 km s^{-1}. The water layer was fixed during the inversion; velocity perturbations were applied only to the part of the model beneath the seafloor.

For the first line modelled (line 15), we used a very simple and smooth starting model based on the geometry seen in a preliminary processed MCS image for this line, which shows a deep basin beneath the GOC, a not-well-imaged but shallower basin structure beneath the GOI and a zone of shallow basement and thin sedimentary cover in-between. Vertical velocity gradients for the starting model were loosely based on the 1-D velocity profiles derived by Clément (2000) from pre-stack depth migration of a Hellenic petroleum MCS profile through the GOI and GOC; he found an average gradient of approximately 1 s^{-1} for the upper 3 km, with a velocity of just over 1.5 km s^{-1} at the seafloor. For subsequent lines, the starting models were based on a simplified, smoothed version of the final model for an adjacent line. We found that the final results were not strongly dependent on the starting model.

A number of methods are available to assess the veracity of tomographic velocity models (Zelt 1999). Besides looking at goodness-of-fit statistics, such as the rms traveltime misfit or normalized χ^2, we also look at the spatial distribution of errors, ray coverage, and perform corrugation tests to gauge the lateral resolution of our data.

We can gain insight into the interpretation of the real data by looking at results from a synthetic test using a velocity model and data that simulate our seismic experiment (Fig. 6). The synthetic model for the test (Fig. 6b) is loosely based on a model for line 15. Taking the 5 km s^{-1} contour to represent the sediment/basement interface, this model includes a deep, bowl-shaped basin in the south, a transition region in the middle with thin sediment cover and another basin in the north with a steep N-dipping southern margin and within which is a floating high-velocity block. The starting model (Fig. 6a) is an actual starting model that was used in the analysis of line 15. We generated ideal synthetic first-arrival traveltime data using the actual line 15 shot–receiver geometry but with no data gaps. Random errors with a standard deviation of 10 ms were added to all traveltimes. The recovered model is shown in Fig. 6(c). We reran this example using more realistic data based on the actual shots and receivers used in the modelling of line 15. Gaussian noise, with a standard deviation equal to the pick uncertainties, was added to the synthetic data. The model recovered using the more realistic data looks nearly identical to the model in Fig. 6(c), suggesting that the

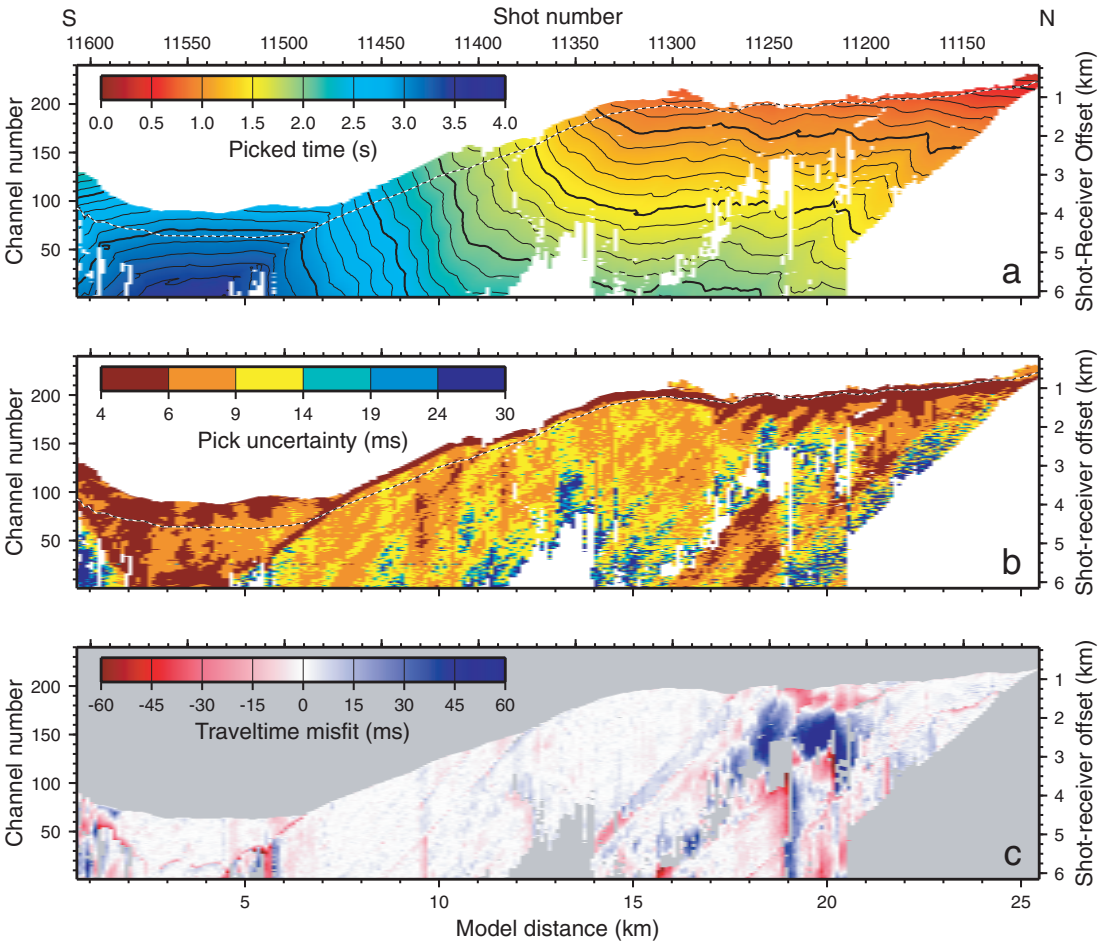

Figure 5. Traveltime data and misfits for line 15. (a) Picked first-arrival traveltimes. A vertical slice through this plot gives the time along the streamer for a single shot. Near offsets (high channel numbers) are at the top of the plot. White regions represent unpicked traces. Broken black and white line shows location where subseafloor refracted arrivals arrive ahead of the direct water wave. Thus picks above this line are not used in the modelling. Contour interval is 0.1 s; heavy lines are 0.5-s contours. (b) Pick uncertainties corresponding to picks shown in (a). An automated routine is used to assign uncertainties between 4 and 25 ms (see text). Relatively low uncertainties between shot points11 500–11 600 corresponds to shots in the deep water of the Corinth basin. (c) Traveltime misfits (calculated minus observed) for the same data shown in (a). Vertical blue or red features correspond to poorly fitting data for a shot gather. Diagonal features correspond to poorly fitting regions that are fixed in space and probably associated with near-surface features. Large misfits between shot points 11 200–11 240 correspond to data recorded when the streamer is within the Gulf of Itea.

data gaps (25 956 versus 30 001 data), which typically occur with our data because of noise, do not significantly affect the tomographic image.

The large-scale features of the true model are well recovered, including the high-velocity anomaly within the northern basin. The shallow velocity structure is more accurately recovered than deeper structure. The variability in the accuracy of the recovered model is closely related to the ray coverage (Fig. 6d), which in turn is dependent on the length of the streamer, depth of water, basin structure and velocity gradients. Ray density is lowest at the south end of the model where the deep water limits the useable data to only the farthest offset receiver channels. Plots of the ray paths for individual shots (Fig. 6e) illustrate this and also show that in deep water the ray paths all turn at approximately the maximum depth of ray coverage. In shallow water at the north end the rays turn through a larger depth range, providing more anisotropic ray coverage and provide better velocity control on the shallow sediments. Note that, in the south, rays do not actually turn below the basement in the deepest part of the basin, which extends to 2.75 km depth. An interpretation based on the recovered model would likely lead to an underestimate of basin depth here. The velocity pull-up at $X = 4$ km, where Xrepresents model distance, is an artefact associated with the transition to dense upgoing ray coverage starting with the southernmost shot. The very high velocity (7 km s^{-1}) region along the steeply N-dipping southern boundary of the deep basin is another artefact related to the very isotropic ray coverage at that location.

5 VELOCITY MODELS

The smoothing regularization inherent in the tomographic method leads to velocity models without discontinuities. Thus, actual discontinuities in seismic velocity are represented by relatively closely spaced isovelocity contours in our displays. Of course, closely spaced contours may also result from a region of relatively high velocity gradient. Our models do not distinguish a high gradient from a sharp discontinuity. Relatively widely spaced contours, on the other hand, likely represent smoothly increasing velocities or a region with small discontinuities.

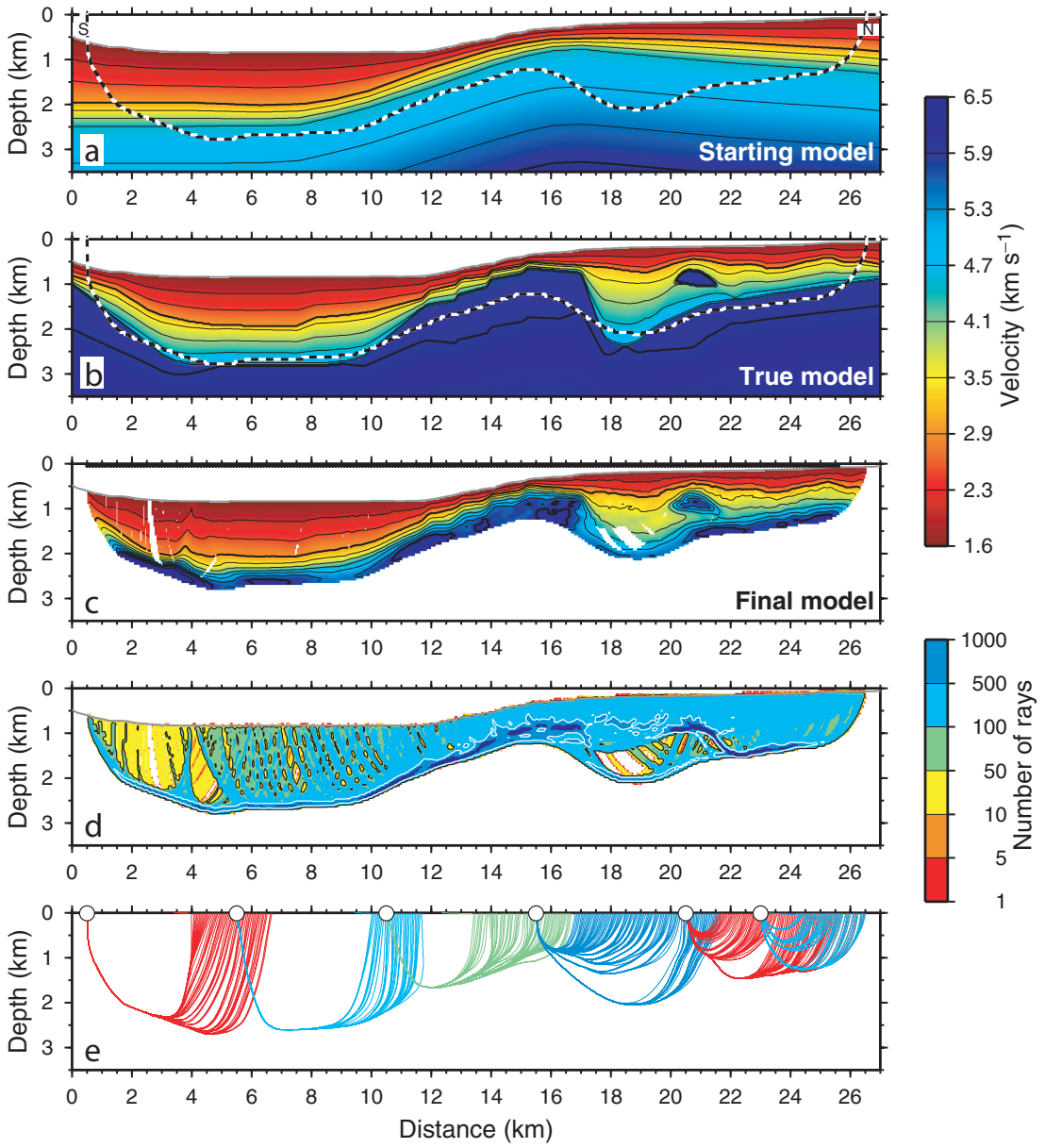

Figure 6. Synthetic streamer tomography test. True model (b) is loosely based on a model for line 15. Noisy synthetic data with the same shot–receiver geometry as used in the real modelling of line 15 were generated using this model. White region at top is water. Contour interval is 0.5 km s^{-1}. Thick black lines are 3 and 6 km s^{-1} contours. Broken black and white line denotes maximum depth extent of model sampled by rays. (a) Starting model is a very simplified and smooth version of the true model. (c) Recovered model. Black dots at top (which appear as a thick line) are shot point locations. White regions are either water (at top) or regions with no ray coverage. (d) Number of rays penetrating each cell of the model. Black and white lines are contours of 50 and 500 rays per cell, respectively. (e) Ray paths for six different shots along the line. Every second ray is plotted. Vertical exaggeration of all plots is 1.5.

5.1 North–south lines 10–17

The eight north–south velocity models (Fig. 7) are grossly similar and each model can be divided laterally into three zones: a southern zone extending from the southern end of each model to approximately $X = 11$–12 km; a central zone that extends to approximately $X = 16$ km; and a northern zone ($X > 16$ km). The southern zone, which represents the main part of the Corinth rift basin, contains the deepest ray coverage (3–3.5 km depth), with velocities increasing from ∼1.5 km s^{-1} at the seafloor to >5 km s^{-1} at the base of ray coverage. There is, in general, a slight increase in vertical velocity gradient for velocities greater than ∼ 4 km s^{-1}, indicating a transition into basement. As we shall show, basement in the southern zone corresponds, on average, to a velocity of approximately 4.5 km s^{-1}. The basin, as outlined by high velocities, appears somewhat bowl-shaped in our velocity models, especially on lines 11, 13 and 15, which sample basement to a larger degree than the other models. The deepest parts of the basin in the east are at approximately 3 km depth, giving a maximum sediment thickness of approximately 2.2 km. On line 17 and other lines to the west, the ray coverage is insufficient to provide a good image of the basement geometry except on the northern margin of the main basin.

The velocity structure within the southern zone is quite similar across all lines, with velocities of 3 km s^{-1} reached at approximately

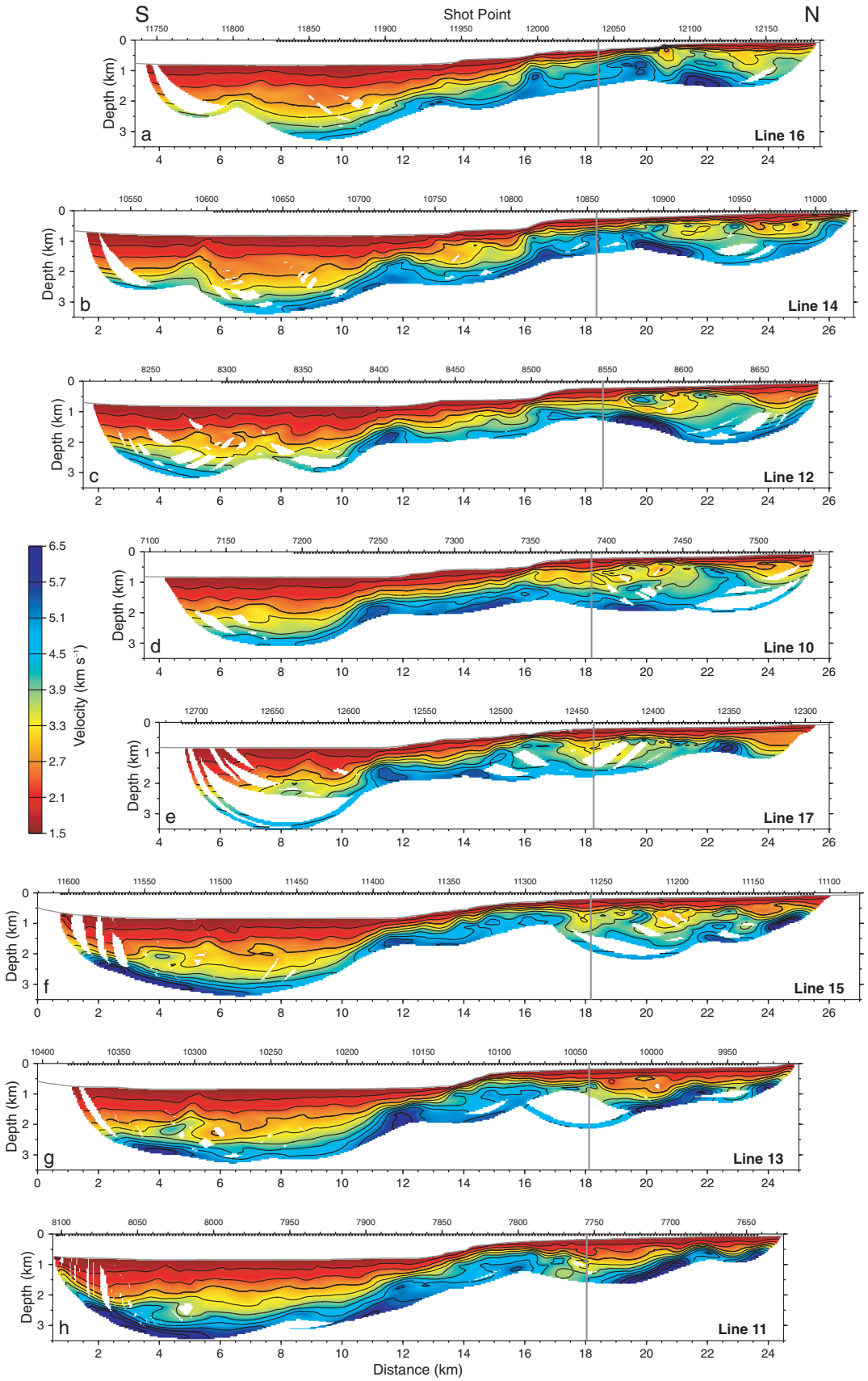

Figure 7. Final models for the eight north–south lines ordered from west (top) to east (bottom). Models are plotted with no vertical exaggeration. Contour interval is 0.5 km s^{-1} ; heavy lines are 3 and 6 km s^{-1} contours. Velocities greater than approximately 4.5 km s^{-1} are considered to represent basement. Dots at top of each plot denote shots used for the modelling. Grey line on each plot (near $X = 18$ km) denotes location of perpendicular line 1.

2 km depth. The shape of the basement at the northern edge of this zone does vary somewhat, dipping more steeply southward on lines 10 and 17 (between $X = 10$–11 km) than on other lines.

The central zone (between approximately $X = 11$ and $X = 16$ km) is a region of elevated basement topography corresponding to the intermediate region between the GOC and GOI where the bathymetry decreases quite rapidly from 800 to 250 m (Fig. 1). The basement in the central part of this region is actually somewhat depressed on lines 12, 14 and 16, forming a fault-bounded terrace adjacent to the main basin to the south. To the east of line 12, the low-velocity sediments in the central zone thin; on lines 15, 13 and 11 there is no suggestion of a thick terrace of sediments in the central zone and, in fact, basement-type velocities occur very near the seafloor.

The northern zone ($X > 16$ km) corresponds to the GOI. In comparison to the relatively simple, smoothly varying west-to-east structure seen further south, the velocity structure in the northern zone shows significantly more lateral variation. In the east, beneath lines 11 and 13, the velocity structure appears relatively simple, with high basement-type velocities dipping to the south. Further west, the velocity structure becomes complicated and, although the line spacing is only ∼1 km, the rapid change of velocities from line to line is indicative of strong lateral heterogeneity within the GOI. A number of small high-velocity (4.5 km s^{-1}) zones embedded in regions with velocities greater than 3 km s^{-1} are further evidence of structural complexity. High basement-type velocities are not consistently reached, suggesting that the basement topography may be somewhat irregular.

5.2 E–W line 1

The velocity structure of the western half of line 1 (Fig. 8a) is relatively flat with velocities increasing to 5 km s^{-1} at approximately 1 km depth. Beginning at the location of line 14 ($X = 19.5$ km), high-velocity contours dip to the east at approximately 20°. East of line 14, the velocity gradient for velocities greater than 3.5 km s^{-1} decreases sharply. We do not image high velocities (>5 km s^{-1}) east of line 10 ($X = 21.5$ km). Depth below seafloor to the 3 km s^{-1} contour increases from ∼250 m west of line 14 to ∼400 m further east. The complex velocity structure beneath the GOI as seen on the N–S slices is also partly mirrored on this E–W slice, with a finger of relatively high (4–4.5 km s^{-1}) velocities dipping to the east at $X = 23.5$ km.

Fig. 8(b) compares the line 1 velocity model with velocities at the intersection points of the eight N–S lines. In general the agreement is good, particularly in the shallow structure where resolution is best. The velocities beneath lines 14 and 16 provide the best match with line 1 probably because the structure here is relatively simple. The somewhat poorer match in deep velocities for lines east of line 14 is a reflection of the complexity of the velocity structure within the GOI. In addition to poor resolution in the deep parts of the models, the discrepancies may, in part, be the result of out of plane sampling caused by dipping high-velocity zones.

6 MODEL ASSESSMENT

Table 1 lists the number of data, final rms traveltime misfit and normalized χ^2 misfit for each line. χ^2 values of 1 imply the data are fit to within the assigned uncertainties in an overall sense, while values greater than 1 imply that data have been underfit. Of the eight north south lines, the two westernmost (16 and 14) and two easternmost lines (13 and 11) are well fit with χ^2 values near 1. Fig. 5(c) exemplifies the distribution of traveltime misfits for the most poorly fitting line (line 15). The region of concentrated large misfits between shot points (11 200–11 240) corresponds to data recorded when the streamer is within the GOI. Plots of misfits for lines 10 and 17 show similar patterns indicative of badly fitting data recorded within the central GOI. The large misfits are not too surprising because the seismic data recorded here are complex; e.g. the first-arrival phase on the gather for shot point 12 459 on line 17 (Fig. 4d) appears to contain two distinct jumps at offsets of 3.4 and 5.0 km, possibly associated with low-velocity zones. Data of this nature are inherently difficult to fit precisely with a tomographic procedure employing smoothness constraints. Both the complexity of the data and the relatively large misfits are consistent with the complex structure seen in the velocity models for the central GOI.

Fig. 9 shows the ray density for each line. Large regions of each model have more than 100 rays per cell. The southern ends of the eight N–S lines consistently have the lowest ray density because in deep water only the very farthest offset traces have subseafloor refracted first arrivals. The ray density beneath the northern ends of some of the lines (14, 12, 10, 17 and 15) is also relatively low suggesting a transition from shallow, high vertical velocity gradients to deeper, low velocity gradients. Ray density is relatively high beneath line 1.

The ability of the data to resolve lateral velocity variations can be gauged by running corrugation tests (e.g. Calvert *et al.* 2003), which are the 2-D equivalent of checkerboard tests commonly used to assess lateral resolution in 3-D tomography problems (Zelt 1998). In the corrugation test, a velocity anomaly pattern comprising fixed-width, vertical columns of alternating positive and negative anomalies are added to the final velocity model to create a perturbed velocity model. Synthetic first-arrival traveltime data are generated using the perturbed velocity model and the same source–receiver geometry of the real data. Gaussian noise with a standard deviation equal to the uncertainty of each pick is added to the synthetic data. The synthetic data are inverted following the same tomographic procedure used for the real data, using the unperturbed, i.e. final, velocity model as the starting model. The difference between the recovered model and the starting model would, if the resolution were perfect, reproduce the velocity anomaly pattern. Regions that do resemble the anomaly pattern indicate where the data is resolving lateral velocity variations of a length scale equal to the anomaly width. Using different anomaly widths gives information on resolution at different length scales.

We show the results of two sets of corrugation tests. In both sets, the magnitude of the velocity anomaly was 10 per cent and four anomaly widths were used: 0.25, 0.5, 1.0 and 2.0 km. The first test was applied to the final model for line 15 (Figs 10a–d). The 0.25-km-wide anomaly pattern is recovered reasonably well to depths of 0.3–0.4 km below the seafloor; however, the amplitude of the recovered anomaly is much weaker in the Corinth basin. This is not surprising given the low ray density at the south end of the model (Fig. 9). Also, in deeper water the first-arriving refracted energy turns deeper and arrives at the surface travelling more nearly vertical (e.g. Fig. 6d). The relatively isotropic ray coverage is not as effective at resolving anomalies. The maximum depth at which the anomaly is well recovered naturally increases with the size of the anomaly. For anomaly widths of 0.5, 1.0, and 2.0 km, the data resolve the anomalies down to depths of approximately 0.5–0.7, 0.6–0.9 and 0.9–1.1 km below the seafloor, respectively.

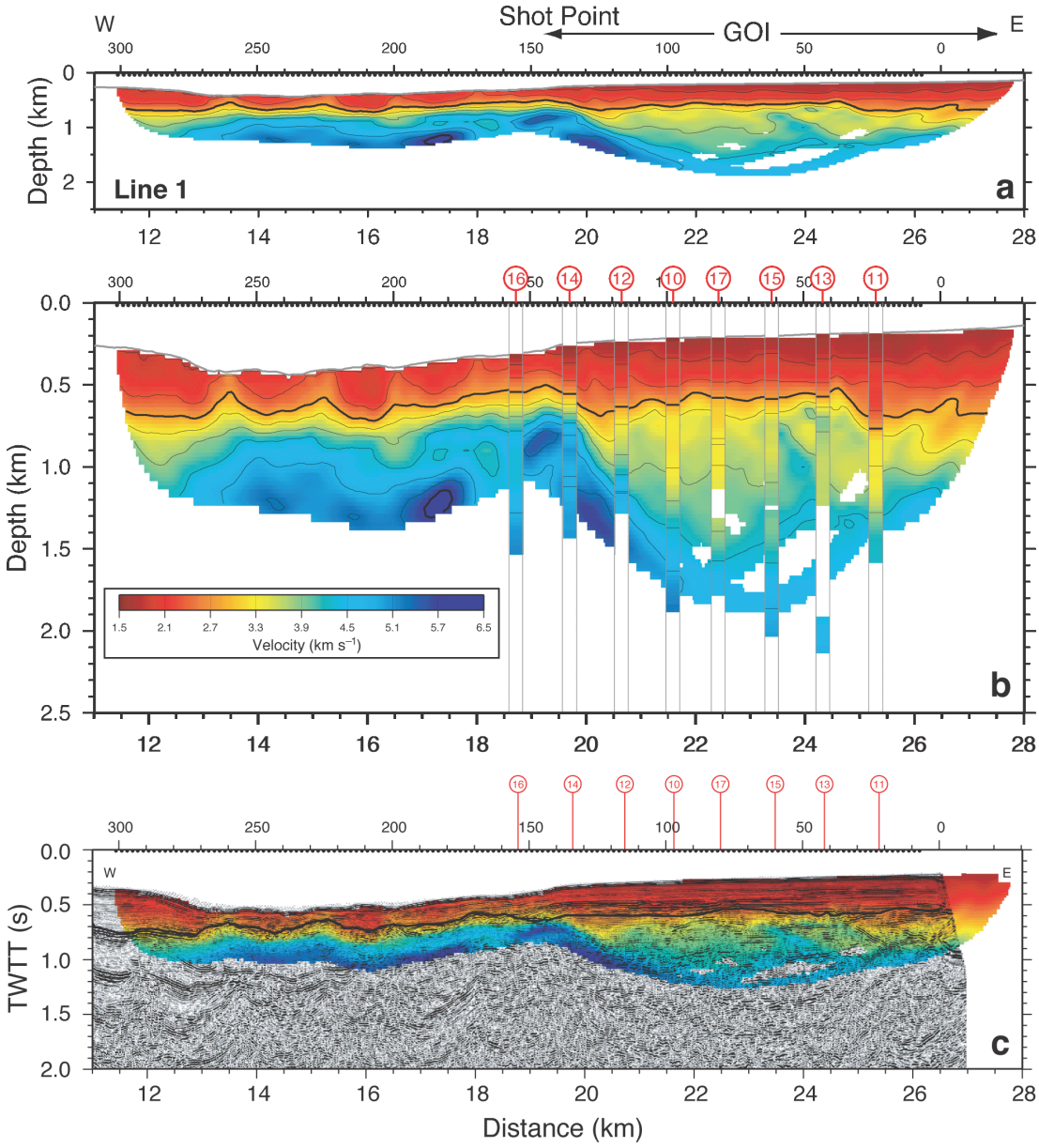

Figure 8. (a) Final model for east–west line 1 plotted with no vertical exaggeration. Contour interval is 0.5 km s^{-1} ; heavy lines are 3 and 6 km s^{-1} contours. Dots at top denote shots used for the modelling. (b) Same as (a) except vertical exaggeration is 2.5. Velocities from the eight north–south crossing lines are plotted on top. Velocities within each column were obtained by taking the 1-D average of the velocity structure in a 0.5-km-wide region about the location of line 1. (c) Velocity superimposed onto time migrated MCS section. Vertical exaggeration is 2.6 at the seafloor. Solid black line represents the rift-onset reflector pick based on reflectivity and velocity. Number in red circles mark the position of the N–S lines presented in Fig. 11.

The second set of corrugation tests were applied to the final model for line 16 (Figs 10e–h). The depths below the seafloor at which the anomalies are well resolved are approximately 0.2–0.4, 0.4–0.8, 0.7–1.0 and 0.9–1.3 km for anomaly sizes of 0.25, 0.5, 1.0 and 2.0 km, respectively. Although the line 16 data are fit significantly better ($\chi^2 = 1.11$ for line 16; $\chi^2 = 2.10$ for line 15), the depth below the seafloor to which the various velocity anomalies are well resolved does not vary greatly. The results presented in Fig. 10 are, in fact, representative of the resolution of the other lines. The main conclusion from these tests is that the lateral resolution of the data is at least 1–2 km down to approximately 1 km below the seafloor. Below this, even large lateral anomalies are not resolved well.

7 INTEGRATION WITH MCS REFLECTION IMAGES: BASEMENT STRUCTURE

In this section, we combine the tomographic velocity models with the coincident, processed MCS sections in order to constrain the depth to the rift-onset reflector. Although the rift-onset reflector can be confidently identified in many places along the MCS profiles, combining the MCS sections with the velocity models allows us to identify the rift-onset reflector across all lines. To this end, we superimposed the velocity models onto the processed, time-migrated MCS sections after first converting the vertical scale of the velocity models to two-way traveltime (Figs 8c and 11).

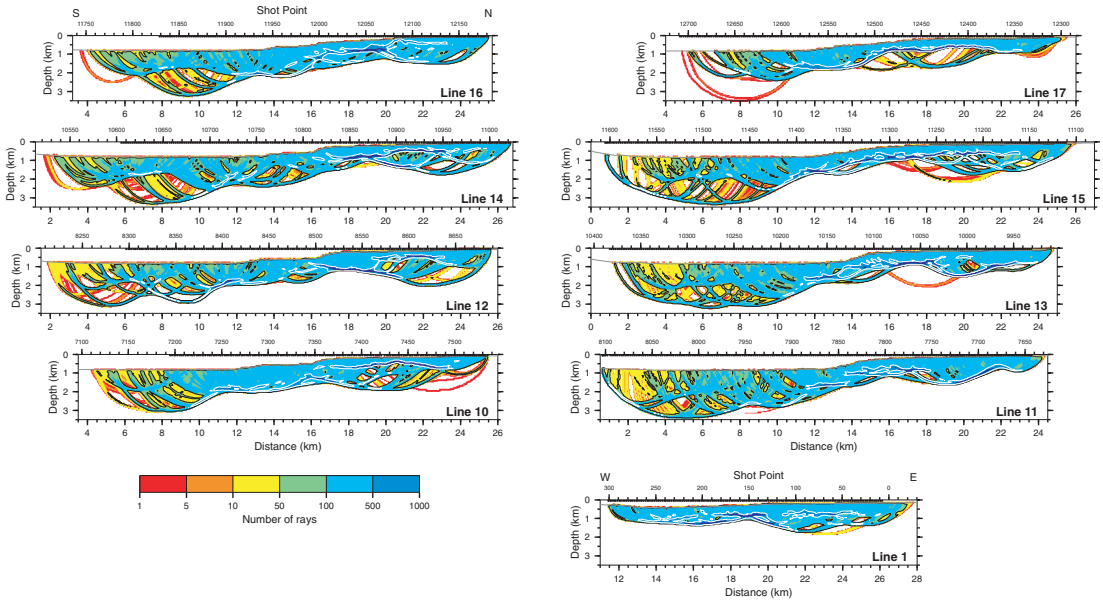

Figure 9. Ray density plots for the nine velocity models plotted with no vertical exaggeration. Black and white lines are contours of 50 and 500 rays per cell, respectively. Black dots at top (which appear as a thick line) are shot point locations. White regions are either water (at top) or regions with no ray coverage.

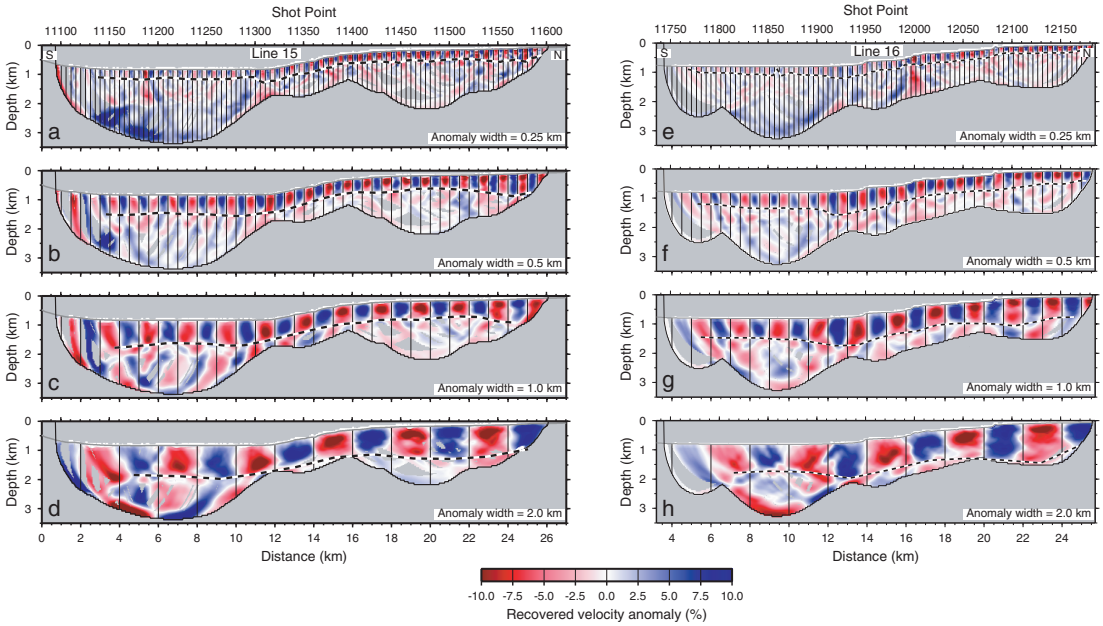

Figure 10. Results of corrugation tests for lines 15 (a–d) and 16 (e–h). True anomaly pattern comprises vertically-oriented columns of alternating ±10 per cent anomalies relative to the true, final model. Vertical lines mark positions where true anomaly is 0 km s^{-1}. Anomaly widths, from top to bottom, are 0.25, 0.5, 1.0 and 2.0 km. Broken black and white line denotes estimate of maximum depth of good resolution.

The N–S MCS profiles (Fig. 11), show a large amount of faulting within the main southern basin. A number of distinct sedimentary sequences have been recognized (Sachpazi *et al.* 2003; Weiss 2004) based on reflectivity; however, if there are distinct velocities associated with any of these packages, the velocity models do not resolve this. A strong package of reflectivity at $\leq$3 s unambiguously demarks basement in the deep part of the main basin. We pick the top of this typically 0.2-s-thick band of reflectivity as the top of the basement. The average velocity along the basement pick in the southern basin is ∼4.5 km s^{-1} ; however, if we factor in the inherent smoothing of velocities across the sediment–basement interface, the actual velocity at or near the top of basement is likely closer to 5.0–5.5 km s^{-1}, consistent with other estimates (Zelt *et al.* 2003; Clément *et al.* 2004).

In the central region between the deep Corinth basin to the south and the GOI to the north, basement shallows along south-dipping normal faults. The basement geometry in this region varies quite substantially across the 7 km between lines 16 and 11, more-or-less echoing the bathymetry between the GOI shelf and Corinth deep (Fig. 1). Basement velocities across the transition region are similar to velocities beneath the deep part of the Corinth basin.

Beneath the GOI, the rift-onset unconformity is subhorizontal and roughly parallel to the gently south-dipping bathymetry. The average velocity along this reflector is 3.1 km s^{-1} and it is not

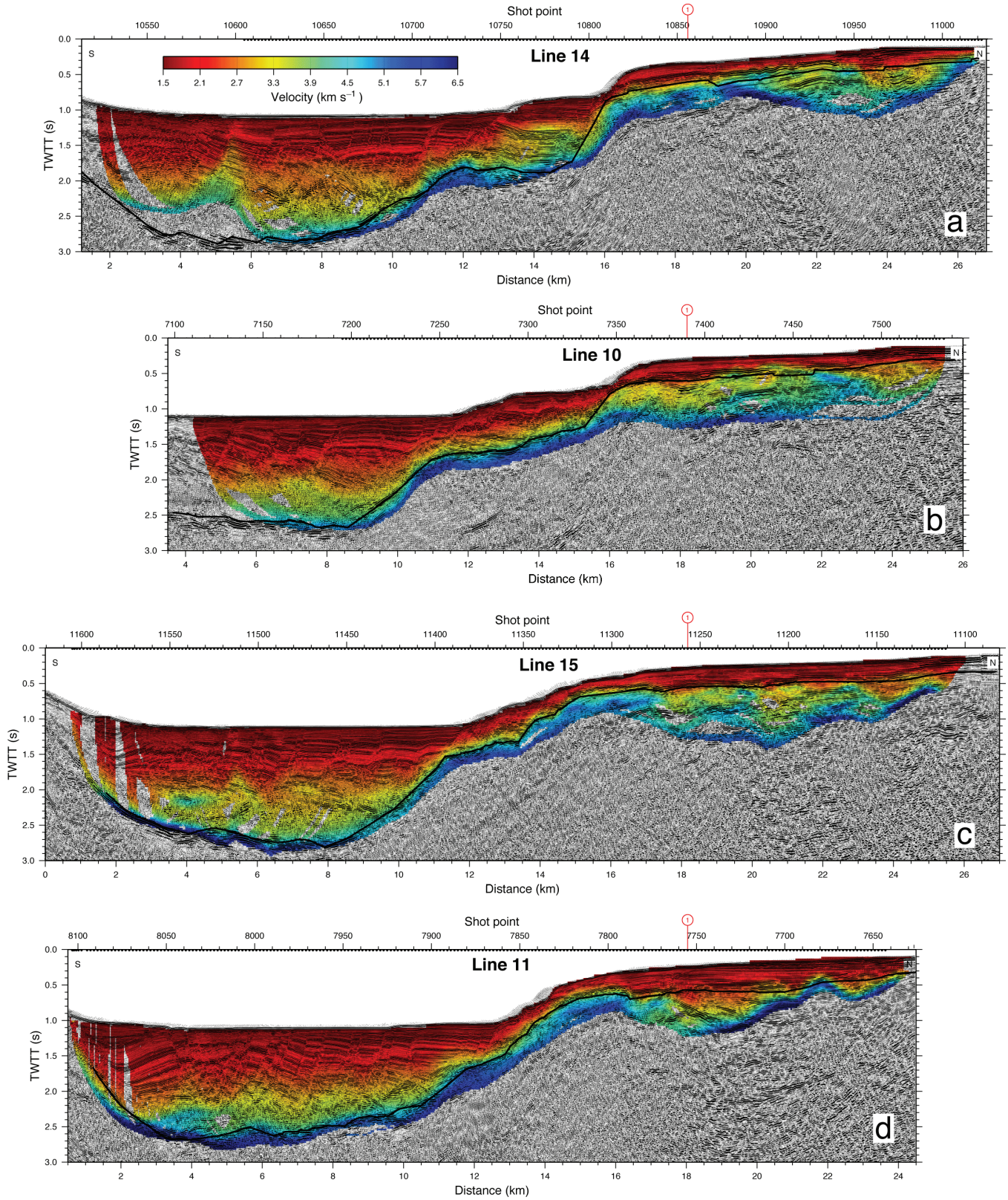

Figure 11. Velocity superimposed onto time migrated MCS sections for every second N–S line, ordered from west (top) to east (bottom). Vertical exaggeration is 2.6 at the seafloor. Solid black line represents the rift-onset unconformity pick based on reflectivity and velocity. The number 1 in a red circle marks the position of the E–W tie line 1 (Fig. 8c).

generally associated with a transition into fast ($\geq$ 5 km s^{-1}) velocities as occurs further south. The low pre-rift velocities here likely represent pre-rift sediments; the GOI may have been a sedimentary basin prior to the current phase of rifting. We do see zones of high, basement-type velocities beneath the GOI and these zones likely correspond to the same basement nappe rocks beneath the GOC to the south. The distribution of these high velocities, however, is quite irregular, suggesting there may be significant topography on this surface. There is no clear correlation between velocity and sub-basement reflectivity in the MCS images, suggesting that either the structure here really is chaotic, or the persistent water multiples obscure weak primary reflections.

The rift-onset reflector on line 1 (Fig. 8c) is approximately flat between 0.6–0.8 s. Mean velocity at this level is 2.8 km s^{-1}, with little variation from west to east. West of line 14, velocities quickly increase to values typically seen in basement beneath the Corinth rift. The low average velocity at this reflector along line 1 may be a result of significantly less compaction compared with the deep Corinth basin. East of line 14, in the GOI, velocities beneath the reflector are low, as we have already seen on the N–S lines, suggesting the presence of pre-rift sediments. High velocities dipping to the east at $\sim$20° between lines 14 and 10 correlate with a dipping reflector that extends down to 1.2 s. The reflector separates pre-rift sediments of the GOI to the east from the high basement velocities further west. It likely formed as a Hellenic thrust that was inverted prior to GOC extension.

8 CONCLUSIONS

We used refracted first-arrival traveltimes recorded along a 6-km MCS streamer to develop 2-D velocity models for several lines within the GOC. Streamer tomography is an attractive method for constraining shallow velocity structure because both the shot and receiver spacing are very close (100 and 25 m, respectively, in our case): an ideal condition for tomography and one that allows for excellent resolution. The closely spaced data also provide the best opportunity for correlating the first-arrival phase from shot to shot, something that is essential for ensuring data consistency. Because the maximum shot–receiver offset is limited by the length of the streamer, only shallow structure can be constrained. In our study, the maximum depth of ray coverage was $\sim$3 km ($\sim$2.2 km below the seafloor), but this value is dependent on the velocity structure. For example, in a sedimentary basin setting such as in the GOC where low velocity sediments are underlain by a high-velocity, low-gradient basement, rays do not penetrate significantly deeper than the top of the basement. An inherent limitation in our method is that only first-arrival traveltimes are useable. Thus, water depth is a critical factor because it governs the minimum offset at which subseafloor refractions arrive ahead of the direct water wave. As an example, given a 6-km streamer length our tomographic procedure could not have been used if water depths were greater than $\sim$1100 m. Conversely, a 3-km-long streamer would have been too short to record any refractions as first arrivals in the deep part of the Corinth basin. Streamer tomography is most effective (i) in shallow water and (ii) using a long streamer; however, in confined bodies of water, such as the GOC, using a streamer longer than 6 km is not practicable.

Velocity models extending across the GOC into the GOI reveal relatively simple and smoothly varying structure from east to west, south of the GOI, and a more complicated structure within the GOI. Integration of the velocity models with migrated MCS sections shows that, on average, basement south of the GOI, which comprises Mesozoic nappes, corresponds to a velocity of 4.5 km s^{-1} in the velocity models, although the actual velocity at, or just below, the top of basement is probably closer to 5.0–5.5 km s^{-1}. Maximum sediment thickness in the Corinth basin is $\sim$ 2.2 km, consistent with estimates from pre-stack depth-migrated MCS images (Sachpazi *et al.* 2003; Clément *et al.* 2004). This is significantly less than the 5 km predicted from the thick elastic plate modelling of Armijo *et al.* (1996), suggesting refinements will be required to their model such that significantly less sedimentation is predicted. Basement shallows to the north into a fault-bounded basement terrace in the central region between the two gulfs. Sediment cover in this central region decreases in thickness from west to east. Beneath the GOI, low average velocities beneath the rift-onset reflector indicate the presence of pre-rift sediments. The deeper velocity structure in the GOI is complex, with significant lateral variation from west to east. High velocities comparable to the basement velocities further south are present beneath the GOI, but the transitions into the high velocities do not correlate with reflectivity on the MCS sections. Where the N–S lines cross an E–W tie line, the velocities at the crossing points are quite similar. The E–W line shows that high-velocity basement is shallow ($\leq$ 1 km depth) and flat to the west of the GOI. These same high velocities dip at approximately 20° to the east beneath the GOI.

ACKNOWLEDGMENTS

Primary funding for this project was from the US NSF, with additional funding from Greece (NOA) and France (CNRS). We thank the scientists and crew of the R/V Maurice Ewing cruise 0108. We thank the Hellenic Coast Guard for facilitating our operations and protecting the 6-km streamer with a chase boat.

REFERENCES

Ambraseys, N. & Jackson, J., 1990. Seismicity and associated strain of Central Greece between 1890 and 1988, *Geophys. J. Int.,* **101,** 663–708.

Armijo, R., Meyer, B., King, G., Rigo, A. & Papanastassiou D., 1996. Quaternary evolution of the Corinth rift and its implications for the late Cenozoic evolution of the Aegean, *Geophys. J. Int.,* **126,** 11–53.

Avallone, A. *et al* 2004. Analysis of eleven years of deformation measured by GPS in the Corinth Rift Laboratory area, *C. R. Geoscience,* **336,** 301–311.

Billiris, H. *et al*., 1991. Geodetic determination of tectonic deformation in Central Greece from 1900 to 1988, *Nature,* **350,** 124–129.

Briole, P. *et al*., 2000. Active deformation of the Gulf of Korinthos, Greece: results from repeated GPS surveys between 1990 and 1995, *J. geophys, Res.,* **105,** 25 605–25 625.

Calvert, A.J., Fisher, M.A., Johnson, S.Y. & SHIPS Working Group, 2003. Along-strike variations in the shallow seismic velocity structure of the Seattle fault zone: evidence for fault segmentation beneath Puget Sound, *J. geophys, Res.,* **108,** 10.1029/2001JB001703.

Clarke, P.J. *et al*., 1997. Geodetic estimate of seismic hazard in the Gulf of Korinthos, *Geophys. Res. Lett.,* **24,** 1303–1306.

Clarke, P. *et al*., 1998. Crustal strain in central Greece from repeated GPS measurements in the interval 1989–1997, *Geophys. J. Int.,* **135,** 195–214.

Clément, C., 2000. Imagerie sismique crustale de la subduction Héllénique et du golfe de Corinthe, *PhD thesis*, University of Paris, Paris.

Clément, C., Sachpazi, M., Charvis, P., Graindorge, D., Laigle, M., Hirn, A. & Zafiropoulos, G., 2004. Reflection-refraction seismics in the Gulf of Corinth: hints at deep structure and control of the deep marine basin, *Tectonophysics,* in press.

Davies, R., England, P., Parson, B., Billiris, H., Paradissis, D. & Veis, G., 1997. Geodetic strain of Greece in the interval 1892–1992, *J. geophys, Res.,* **102,** 24 571–24 588.

Goldsworthy, M., Jackson, J. & Haines, J., 2002. The continuity of active fault systems in Greece, *Geophys. J. Int.,* **148,** 596–618.

Goodliffe, A.M., Weiss, J.R., Taylor, B., Sachpazi, M., Hirn, A., Stefatos, A. & Laigle, M., 2003. Variations in the distribution and control of syn-rift deformation in the Gulf of Corinth, Greece, *Geophysical Research Abstracts,* **5,** 04697.

Hatzfeld, D. *et al*., 1996. The Galaxidi earthquake of November 18, 1992: a possible asperity within the normal fault system of the Gulf of Corinth (Greece), *Bull. seism. Soc. Am.,* **86,** 1987–1991.

Hatzfeld, D., Karakostas, V., Ziazia, M., Kassaras, I., Papadimitriou, E., Makropoulos, K., Voulgaris, N. & Papaioannou, C., 2000. Microseismicity and faulting geometry in the Gulf of Corinth (Greece), *Geophys. J. Int.,* **141,** 438–456.

Hole, J.A. & Zelt, B.C., 1995. Three-dimensional finite-difference reflection traveltimes, *Geophys. J. Int.,* **121,** 427–434.

Jolivet, L., 2001. A comparison of geodetic and finite strain pattern in the Aegean, geodynamic implications, *Earth planet. Sci. Lett.,* **187,** 95–104.

Le Pourhiet, L., Burov, E. & Moretti, I., 2003. Initial crustal thickness geometry controls on the extension in a back arc domain: case of the Gulf of Corinth, *Tectonics,* **22,** 10.1029/2002TC001433.

McClusky, S. *et al*., 2000. Global Positioning System constraints on plate kinematics and dynamics in the eastern Mediterranean and Caucasus, *J. geophys, Res.,* **105,** 5695–5719.

Moretti, I., Sakellariou, D., Lykousis, V. & Micarelli, L., 2003. The Gulf of Corinth: an active half graben?, *J. Geodyn.,* **36,** 323–340.

Rietbrock, A., Tiberi, C., Scherbaum, F. & Lyon-Caen, H., 1996. Seismic slip on a low angle normal fault in the Gulf of Corinth: evidence from high resolution cluster analysis of microearthquakes, *Geophys. Res. Lett.,* **14,** 1817–1820.

Rigo, A., Lyon-Caen, H., Armijo, R., Deschamps, A., Hatzfeld, D., Makropoulos, K., Papadimitriou, P. & Kassaras, I., 1996. A microseismic study in the western part of the Gulf of Corinth (Greece): implications for large-scale normal faulting mechanisms, *Geophys. J. Int.,* **126,** 663–688.

Sachpazi, M., Clément, C., Laigle, M., Hirn, A. & Roussos, N., 2003. Rift structure, evolution, and earthquakes in the Gulf of Corinth, from reflection seismic images, *Earth planet. Sci. Lett.,* **216,** 243–257.

Taylor, B., Goodliffe, A., Weiss, J., Sachpazi, M., Hirn, A., Laigle, M. & Stefatos, A., 2003. Detachment tectonics in the Gulf of Corinth rift, *Geophysical Research Abstracts,* **5,** 07222.

Vidale, J.E., 1990. Finite-difference calculation of traveltimes in three dimensions, *Geophysics,* **55,** 521–526.

Weiss, J.R., 2004. A geophysical investigation of the Gulf of Corinth, Greece, *MSc thesis,* University of Hawaii, Honolulu.

Weiss, J.R., Taylor, B., Goodliffe, A.M., Hirn, A., Sachpazi, M., Stefatos, A. & Laigle, M., 2003. Fault-controlled sedimentation in the Gulf of Corinth, Greece, *Geophysical Research Abstracts,* **5,** 07036.

Zelt, C.A., 1998. Lateral velocity resolution from three-dimensional seismic refraction data, *Geophys. J. Int.,* **135,** 1101–1112.

Zelt, C.A., 1999. Modelling strategies and model assessment for wide-angle seismic traveltime data, *Geophys. J. Int.,* **139,** 183–204.

Zelt, C.A. & Barton, P.J., 1998. Three-dimensional seismic refraction tomography: a comparison of two methods applied to data from the Faeroe Basin, *J. geophys, Res.,* **103,** 7187–7210.

Zelt, C.A. & Forsyth, D.A., 1994. Modeling wide-angle seismic data for crustal structure: southeastern Grenville province, *J. geophys, Res.,* **99,** 11 687–11 704.

Zelt, B.C., Taylor, B., Hirn, A. & Sachpazi, M., 2003. Deep crustal and shallow sedimentary velocity structure along the Gulf of Corinth rift, *Geophysical Research Abstracts,* **5,** 04679.